Optimization of the interface distortion of a round liquid jet

By H. Hwang AND M. J. P. Hack

1. Motivation and objectives

A comprehensive physics-based description of the atomization process has been a long-standing and a challenging engineering problem of a fundamental interest. An accurate control of the atomization process based on understanding of underlying physics is desired in the internal combustion engine community in order to develop more efficient engines as well as in other areas such as medicine for more accurate medical devices development. Even though multi-physics and a wide range of scales made this problem extremely difficult to solve, many researchers have dedicated to experiments and analytical studies to provide a consistent description of an instability process of the liquid jet. Traditionally, prediction of relevant wavelength, wave velocity and growth rate is discussed in a relatively simpler cases, for example, inviscid flow with piecewise linear base profile.

The atomization of a liquid jet can be separated into primary and secondary atomization. Primary atomization describes the distortion and eventual disintegration of the jet by external force or by instability mechanisms and leads to comparatively large fragments of liquid. In the following secondary atomization stage, these large drops undergo further breakup into increasingly smaller droplets. Primary atomization often occurs in relative vicinity of the nozzle exit. Therefore, initial conditions, such as perturbations to the flow inside the nozzle as well as the nozzle geometry, have to be considered in descriptions of primary atomization (see, e.g. Huh *et al.* 1998; Senecal *et al.* 1999).

The velocity difference between the liquid jet and the surrounding gas environment gives rise to an inviscid shear instability of Kelvin-Helmholtz(KH) type. Experiments by Marmottant & Villermaux (2004) visualized the KH instability as an axisymmetric perturbation of the liquid interface. They propose that the instability would be predicted by the most unstable mode computed in a simplified linear stability analysis assuming a planar interface. Linear stability theory has been indeed extensively applied to predict the length scales of primary atomization (see., e.g. Lin & Ibrahim 1990; Preziosi *et al.* 1989; Hu & Joseph 1989). After the initial distortion of the jet interface by the Kelvin-Helmholtz instability, the jet commonly undergoes a secondary instability of Rayleigh-Taylor (RT) type instability which introduces an azimuthally inhomogeneous deformation of the material interface and leads to the eventual separation of individual droplets by capillary Plateau-Rayleigh instability. The detailed simulations by Kim & Moin (2011) confirm this sequence of events. It should be noted that for sufficiently low Weber numbers, the jet may alternatively also disintegrate via the Plateau-Rayleigh instability in the absence of a shear-layer instability (see Lasheras & Hopfinger 2000).

Even when linear stability analysis predicts a flow to be exponentially stable, perturbations can amplify appreciably by extracting kinetic energy from the mean shear. This process is known as transient growth or non-modal growth and was originally considered in single-phase shear flows (see., e.g. Gustavsson 1991; Trefethen *et al.* 1993). More re-

cently, Jiménez-González & Brancher (2017) investigated optimal streak intensity with different azimuthal wavenumbers. The identification of the transiently most amplified perturbations can be cast into an optimization problem which is solved by means of singular value decomposition of the linearized governing equations. One of the first applications of the concept to two-fluid flows was conducted by (South & Hooper 1999), who computed optimal disturbances in terms of a norm that accounts for the potential energy stored in the interface owing to surface tension. van Noorden *et al.* (1998); Yecko & Zaleski (2005); Malik & Hooper (2007); Boronin *et al.* (2013) followed the framework of two-phase transient growth addressing the importance of including interface potential energy. These studies nonetheless follow the original single-phase investigations of non-modal growth in effectively maximizing the kinetic energy of disturbances, augmented by a contribution of the interface energy that is motivated to improve the convergence of the optimization algorithm.

Our study aims to identify for the first time the specific disturbances which maximize the distortion of the material interface, and as such advance the atomization process. To this aim, we introduce a novel choice for the objective functional of the optimization problem is defined. The spatial stability of the flow is determined using the eigenfunctions of the adjoint system. The prediction of the linear stability analysis is compared and verified with computer simulations using the Basilisk (Popinet 2015, 2018) code based on a geometric volume of fluid formulation.

2. Methodology

In the following, we describe a conceptual framework for the analysis of linearly amplifying distortions in the shear layer surrounding a liquid jet in a quiescent gas medium. The formulation considers the effects of viscosity as well as surface tension under the assumption of an axisymmetric laminar base state.

2.1. *Nondimensional parameters*

The radius, R, and the local centerline velocity, U_c, of the jet are chosen as the characteristic length and velocity in this work. The Weber number and the Reynolds number are defined based on the parameters of the liquid phase. Including the viscosity ratio, m, and the density ratio, η, the four independent parameters of the system are thus

$$m = \frac{\mu_g}{\mu_l}, \qquad \eta = \frac{\rho_g}{\rho_l}, \qquad Re_l = \frac{\rho_l U_c R}{\mu_l}, \qquad We = \frac{\rho_l U_c^2 R}{\sigma}. \tag{2.1}$$

2.2. *Linear stability equations*

The dynamics of the perturbations considered within this work are governed by the linearized Navier-Stokes equations in cylindrical coordinates where z, r and θ denote the axial, radial and azimuthal directions, respectively. The axial expansion of the jet is assumed to be small and as such is disregarded in the following, leading to a base flow of the form $\boldsymbol{U} = [U(r), 0, 0]^{\mathsf{T}}$. Linearization of the Navier-Stokes equations for each fluid phase leads to

$$\frac{\partial u}{\partial t} + U\frac{\partial u}{\partial z} = -\frac{\partial p}{\partial z} + \frac{1}{Re}\nabla^2 u, \tag{2.2}$$

$$\frac{\partial v}{\partial t} + U\frac{\partial v}{\partial z} + vU' = -\frac{\partial p}{\partial r} + \frac{1}{Re}\left(\nabla^2 v - \frac{v}{r^2} - \frac{2}{r^2}\frac{\partial w}{\partial \theta}\right), \tag{2.3}$$

$$\frac{\partial w}{\partial t} + U\frac{\partial w}{\partial z} = -\frac{1}{r}\frac{\partial p}{\partial \theta} + \frac{1}{Re}\left(\nabla^2 w + \frac{2}{r^2}\frac{\partial v}{\partial \theta} - \frac{w}{r^2}\right), \tag{2.4}$$

$$\frac{\partial u}{\partial z} + \frac{1}{r}\frac{\partial}{\partial r}(rv) + \frac{\partial w}{\partial \theta} = 0, \tag{2.5}$$

where u, v and w are the velocity disturbances in the axial, radial and azimuthal directions, respectively, and U' denotes the derivative of the base flow in the radial direction. In contrast to formulations in terms of the radial velocity and vorticity as proposed for instance in Schmid & Henningson (1994), the present formulation, Eqs. (2.2)–(2.5), are second order equations with respect to the streamwise derivative.

Homogeneity of the base flow in the x, θ and t dimensions allows a normal-mode ansatz for the disturbances, which are assumed to have the form

$$[u, v, w, p] = [\widehat{u}(r), \mathrm{i}\widehat{v}(r), \widehat{w}(r), \widehat{p}(r)]\, \mathrm{e}^{\mathrm{i}(\alpha z + n\theta - \omega t)}, \tag{2.6}$$

where α and n denote the streamwise and discrete azimuthal wavenumber, respectively, and ω represents the frequency of the disturbance. The spatial discretization in the inhomogeneous radial dimension, r, uses the Chebyshev collocation method for each phase. Substitution of the ansatz, Eq. (2.6), into the governing equations, Eqs. (2.2)–(2.5), results in the following set of equations

$$\left\{-\frac{1}{Re}\frac{\mathrm{d}^2}{\mathrm{d}y^2} - \frac{1}{Re}\frac{1}{r}\frac{\mathrm{d}}{\mathrm{d}y} + \left[-\mathrm{i}\omega + \mathrm{i}\alpha U + \frac{1}{Re}\left(\frac{n^2+1}{r^2} + \alpha^2\right)\right]\right\}\widehat{u} + \frac{1}{Re}\frac{2n}{r^2}\widehat{v} + \frac{\mathrm{i}n}{r}\widehat{p} = 0, \tag{2.7}$$

$$\left\{-\frac{\mathrm{i}}{Re}\frac{\mathrm{d}^2}{\mathrm{d}y^2} - \frac{\mathrm{i}}{Re}\frac{1}{r}\frac{\mathrm{d}}{\mathrm{d}y} + \left[\omega - \alpha U + \frac{\mathrm{i}}{Re}\left(\frac{n^2+1}{r^2} + \alpha^2\right)\right]\right\}\widehat{v} + \frac{1}{Re}\frac{\mathrm{i}2n}{r^2}\widehat{u} + \frac{\mathrm{d}\widehat{p}}{\mathrm{d}y} = 0, \tag{2.8}$$

$$\left\{-\frac{1}{Re}\frac{\mathrm{d}^2}{\mathrm{d}y^2} - \frac{1}{Re}\frac{1}{r}\frac{\mathrm{d}}{\mathrm{d}y} + \left[-\mathrm{i}\omega + \mathrm{i}\alpha U + \frac{1}{Re}\left(\frac{n^2}{r^2} + \alpha^2\right)\right]\right\}\widehat{w} + \mathrm{i}U'\frac{\mathrm{d}\widehat{v}}{\mathrm{d}y} + \mathrm{i}\alpha\widehat{p} = 0, \tag{2.9}$$

$$\frac{n}{r}\widehat{u} + \left(\frac{\mathrm{d}}{\mathrm{d}y} + \frac{1}{r}\right)\widehat{v} + \alpha\widehat{w} = 0. \tag{2.10}$$

The disturbance of the interface between the two phases is represented by the complex interface displacement, $\widehat{f}$. The interface disturbance is assumed to be small and satisfies the following kinematic condition

$$\frac{\mathrm{d}f}{\mathrm{d}t} = \left(\frac{\partial}{\partial t} + U\frac{\partial}{\partial z}\right)\widehat{f} = \left(-\mathrm{i}\omega + \mathrm{i}\alpha U_l^I\right)\widehat{f} = v_l^I. \tag{2.11}$$

Here, the superscript I denotes quantities evaluated at the interface.

2.3. *Spatial linear analysis*

The stability equations Eqs. (2.7)–(2.10) permit solutions of both spatially and temporally growing solutions. While temporal stability analysis is conceptually simpler, it is less appropriate in the analysis of disturbances that are generated at a fixed position in space. Within the framework of spatial stability analysis, the frequency ω and the azimuthal wavenumber n of the disturbances of interest are prescribed, real quantities. As a consequence, only certain, generally complex α satisfy the stability equations Eqs. (2.7)–(2.10), thus giving rise to an eigenvalue problem of the form

$$\mathrm{i}\alpha\mathsf{M}\widehat{\boldsymbol{q}} = \mathsf{L}\widehat{\boldsymbol{q}}. \tag{2.12}$$

Here, $\widehat{\boldsymbol{q}}$ is the disturbance state vector

$$\widehat{\boldsymbol{q}} = \begin{bmatrix} \widehat{\phi}_g(y) & \widehat{f} & \widehat{F} & \widehat{\phi}_l(y) \end{bmatrix}^{\mathsf{T}}, \tag{2.13}$$

where the indices g and l respectively denote the gas and liquid phases, and

$$\widehat{\phi}_i = \begin{bmatrix} \widehat{u}_i(y) & \widehat{v}_i(y) & \widehat{w}_i(y) & \widehat{p}_i(y) & \widehat{U}_i(y) & \widehat{V}_i(y) & \widehat{W}_i(y) \end{bmatrix}^{\mathsf{T}}. \tag{2.14}$$

Further,

$$\mathsf{M} = \begin{pmatrix} \widetilde{\mathsf{M}} & 0 & 0 & 0 \\ 0 & 1 & 0 & 0 \\ 0 & -\mathrm{i} & 0 & 0 \\ 0 & 0 & 0 & \widetilde{\mathsf{M}} \end{pmatrix}, \quad \mathsf{L} = \begin{pmatrix} \mathsf{L}_j & 0 & 0 & 0 \\ 0 & \mathrm{i}\omega & 0 & \widetilde{\mathsf{L}} \\ 0 & 0 & 1 & 0 \\ 0 & 0 & 0 & \mathsf{L}_j \end{pmatrix}. \tag{2.15}$$

The block matrices $\widetilde{\mathsf{M}}$, $\widetilde{\mathsf{L}}$ and L_j are defined as

$$\widetilde{\mathsf{M}} = \begin{pmatrix} 0 & 0 & U_j & 1 & 0 & 0 & \frac{\mathrm{i}}{Re_j} \\ -\mathrm{i}U_j & 0 & 0 & 0 & \frac{1}{Re_j} & 0 & 0 \\ 0 & U_j & 0 & 0 & 0 & \frac{\mathrm{i}}{Re_j} & 0 \\ \mathrm{i} & 0 & 0 & 0 & 0 & 0 & 0 \\ 0 & 0 & -\mathrm{i} & 0 & 0 & 0 & 0 \\ -\mathrm{i} & 0 & 0 & 0 & 0 & 0 & 0 \\ 0 & -\mathrm{i} & 0 & 0 & 0 & 0 & 0 \end{pmatrix}, \tag{2.16}$$

$$\mathsf{L}_j = \begin{pmatrix} \mathrm{i}\frac{\mathrm{d}U_j}{\mathrm{d}y} & 0 & \mathcal{U}_j & 0 & 0 & 0 & 0 \\ \mathcal{V}_j & -\mathrm{i}\frac{1}{Re_j}\frac{2n}{r^2} & 0 & \frac{\mathrm{d}}{\mathrm{d}y} & 0 & 0 & 0 \\ \frac{1}{Re_j}\frac{2n}{r^2} & \mathcal{W}_j & 0 & \mathrm{i}\frac{n}{r} & 0 & 0 & 0 \\ \mathcal{P}_j & \frac{n}{r} & 0 & 0 & 0 & 0 & 0 \\ 0 & 0 & 0 & 0 & 0 & 0 & 1 \\ 0 & 0 & 0 & 0 & 1 & 0 & 0 \\ 0 & 0 & 0 & 0 & 0 & 1 & 0 \end{pmatrix}, \tag{2.17}$$

$$\widetilde{\mathsf{L}} = [0 \quad \mathrm{i} \quad 0 \quad 0 \quad 0 \quad 0 \quad 0], \tag{2.18}$$

and the elements of the matrices L_j are

$$\mathcal{U}_j = -\frac{1}{Re_j}\frac{\mathrm{d}^2}{\mathrm{d}y^2} - \frac{1}{Re_j}\frac{1}{r}\frac{\mathrm{d}}{\mathrm{d}y} + \left(-\mathrm{i}\omega + \frac{1}{Re_j}\frac{n^2}{r^2}\right), \tag{2.19}$$

$$\mathcal{V}_j = -\frac{\mathrm{i}}{Re_j}\frac{\mathrm{d}^2}{\mathrm{d}y^2} - \frac{\mathrm{i}}{Re_j}\frac{1}{r}\frac{\mathrm{d}}{\mathrm{d}y} + \left\{\omega + \frac{\mathrm{i}}{Re_j}\left(\frac{n^2+1}{r^2}\right)\right\}, \tag{2.20}$$

$$\mathcal{W}_j = -\frac{1}{Re_j}\frac{\mathrm{d}^2}{\mathrm{d}y^2} - \frac{1}{Re_j}\frac{1}{r}\frac{\mathrm{d}}{\mathrm{d}y} + \left\{-\mathrm{i}\omega + \frac{1}{Re_j}\left(\frac{n^2+1}{r^2}\right)\right\}, \tag{2.21}$$

$$\mathcal{P}_j = \frac{\mathrm{d}}{\mathrm{d}y} + \frac{1}{r}, \tag{2.22}$$

Note that the Reynolds numbers in Eqs. (2.19)–(2.21) are related through $Re_g = (\eta/m)Re_l$.

No-slip and no-penetration boundary conditions are imposed on the eigenfunctions in the far field of the gas phase. At the interface, velocities and tangential stresses are

prescribed to be continuous and the normal stress follows a prescribed offset. The reader is referred to Hwang & Hack (2018) for detailed expressions for both boundary and interface conditions.

2.4. *Optimization problem*

The solution of the spatial eigenvalue problem Eq. (2.12) leads to solutions which are either exponentially amplifying or decaying. However, even when all the eigensolutions are decaying, the non-normal nature of the linearized Navier-Stokes equations provides a pathway for disturbance growth. The study of this non-modal, or transient, amplification of disturbances can be solved in terms of an optimization problem in a suitably chosen norm. The main aspects have been documented in Hwang & Hack (2018), and are only briefly revisited in the following.

Since we are interested in the conditions which allow the amplification of distortions in the liquid/gas interface of the jet, we introduce an interface energy norm of the form

$$||q||_{IE} = \int_{\theta=0}^{\theta=2\pi} \int_{0}^{\frac{2\pi}{\omega}} \left[B\widehat{f}^2\right]_{r'=1} \mathrm{d}t\mathrm{d}\theta. \tag{2.23}$$

Here, B is a coefficient, which will be discussed in detail in the following section. The introduction of a weight matrix F allows the transformation of the interface energy norm into a 2-norm so that $||\boldsymbol{q}||_{IE} \equiv ||\mathsf{F}\boldsymbol{q}||_2$. The norm, Eq. (2.23), partitions the state vector and as such describes a nontrivial semi-norm with F rank-deficient. Specifically, the velocity and pressure components of both the gas and the liquid phases are within the kernel of F. The formulation of a well-posed optimization problem thus calls for the introduction of a full norm (see e.g. Foures *et al.* 2012), which is chosen to be the total energy norm

$$\begin{aligned} ||q||_E = \frac{1}{2}\Big[\eta \int_{r'=1}^{r'=L_g} \int_{\theta=0}^{\theta=2\pi} \int_{0}^{\frac{2\pi}{\omega}} \left(|\widehat{u}_g|^2 + |\widehat{v}_g|^2 + |\widehat{w}_g|^2\right) r' \mathrm{d}t\mathrm{d}r'\mathrm{d}\theta \\ + \int_{r'=0}^{r'=1} \int_{\theta=0}^{\theta=2\pi} \int_{0}^{\frac{2\pi}{\omega}} \left(|\widehat{u}_l|^2 + |\widehat{v}_l|^2 + |\widehat{w}_l|^2\right) r' \mathrm{d}t\mathrm{d}r'\mathrm{d}\theta\Big] + ||q||_{IE}. \end{aligned} \tag{2.24}$$

Analogous to the interface energy norm, the energy norm can be converted to a 2-norm by means of the matrix F_N, with $||\boldsymbol{q}||_E \equiv ||\mathsf{F}_N\boldsymbol{q}||_2$. Since Eq. (2.24) takes into account all components of the state vector, the null space of F_N is empty. The optimal initial and final conditions can be expressed as

$$\mathbf{q}_0 = \mathsf{Q}_0\boldsymbol{\kappa}, \qquad \mathbf{q}_1 = \mathsf{Q}_1\boldsymbol{\kappa}, \tag{2.25}$$

where the columns of Q_0 and Q_1 comprise the N least stable eigenfunctions at the initial and final location and $\boldsymbol{\kappa}$ assigns each of those modes a specific weight. The linear nature of the problem implies that $\boldsymbol{\kappa}$ is identical in both expressions. Since Q_0 has full column rank, we can directly compute its pseudoinverse Q_0^+, leading to

$$\mathsf{Q}_0^+\mathsf{q}_0 = \boldsymbol{\kappa}. \tag{2.26}$$

Substitution into Eq. (2.25) yields

$$\mathbf{q}_1 = \mathsf{Q}_1\mathsf{Q}_0^+\mathbf{q}_0 = \mathcal{L}_1\mathbf{q}_0, \tag{2.27}$$

where $\mathcal{L}_1$ is a pseudo-propagator that advances arbitrary initial disturbances $\mathbf{q}_0$ within the column space of Q_0 from x_0 to x_1. The objective of finding the specific initial condition

$\boldsymbol{q}_0$ that maximizes the magnitude of interface distortions at a given target location x_1 may thus be expressed as the functional

$$\begin{aligned} G(x_1) &= \max_{\boldsymbol{q}_0} \frac{||\boldsymbol{q}_1||_{IE}^2}{||\boldsymbol{q}_0||_E^2} = \max_{\boldsymbol{q}_0} \frac{||\mathcal{L}_1\boldsymbol{q}_0||_{IE}^2}{||\mathcal{L}_0\boldsymbol{q}_0||_E^2} = \max_{\boldsymbol{q}_0} \frac{||\mathsf{F}\mathcal{L}_1\boldsymbol{q}_0||_2^2}{||\mathsf{F}_N\mathcal{L}_0\boldsymbol{q}_0||_2^2} \\ &= \max_{\boldsymbol{q}_0} \frac{||\mathsf{F}\mathcal{L}_1(\mathsf{F}_N\mathcal{L}_0)^+\mathsf{F}_N\mathcal{L}_0\boldsymbol{q}_0||_2^2}{||\mathsf{F}_N\mathcal{L}_0\boldsymbol{q}_0||_2^2} = ||\mathsf{F}\mathcal{L}_1(\mathsf{F}_N\mathcal{L}_0)^+||_2^2. \end{aligned} \tag{2.28}$$

Note that $\boldsymbol{q}_1 = \boldsymbol{q}(x_1)$ and the introduction of $\mathcal{L}_0 = \mathsf{Q}_0\mathsf{Q}_0^+$ into the denominator restricts $\mathbf{q}_0$ to the column space of Q_0.

2.5. *Interface energy norm*

The present work seeks to identify the specific disturbances which amplify the distortion of the material interface most effectively. This aim is reflected in the choice of the objective functional of the optimization problem which follows the form introduced in Eq. (2.23). The choice of B affects the energy gain by a large factor as shown in Boronin *et al.* (2013). Since present study take into account the effects of surface tension, the coefficient, B, in Eq. (2.23) is chosen considering the physical interface topology. We start from the definition of interface energy norm.

$$E_{interface} = \int_0^{\lambda}\int_0^{2\pi} -\sigma\kappa f \mathrm{d}S, \tag{2.29}$$

where f is a physical interface distortion displacement which has a form of normal disturbance as $f = \widehat{f}\, e^{\mathrm{i}\omega t + \mathrm{i}n\theta + \mathrm{i}\alpha x}$. We further introduce the level-set function H as

$$H = r - f(x,\ \theta) = r - \left(1 + \widehat{f} e^{\mathrm{i}\omega t + \mathrm{i}n\theta + \mathrm{i}\alpha x}\right). \tag{2.30}$$

The curvature of the liquid interface may then be expressed in terms of H as

$$\nabla H = \frac{\partial H}{\partial r}\widehat{r} + \frac{1}{r}\frac{\partial H}{\partial \theta}\widehat{\theta} + \frac{\partial H}{\partial x}\widehat{x} = \widehat{r} + \frac{\mathrm{i}n}{r} f\widehat{\theta} + \mathrm{i}\alpha f\widehat{x}, \tag{2.31}$$

and Laplacian operator on H follows

$$\nabla^2 H = \frac{1}{r}\frac{\partial}{\partial r}\left(r\frac{\partial H}{\partial r}\right) + \frac{1}{r^2}\frac{\partial^2 H}{\partial \theta^2} + \frac{\partial^2 H}{\partial x^2} = \frac{1}{r} - \frac{n^2}{r^2} f - \alpha^2 f. \tag{2.32}$$

Note that the infinitesimal surface area $\mathrm{d}S$

$$\mathrm{d}S = \left\{1 + \left(\frac{\partial f}{\partial x}\right)^2 + \left(\frac{\partial f}{\partial \theta}\right)^2\right\}^{\frac{1}{2}} = |\nabla H|\ \mathrm{d}x\mathrm{d}\theta. \tag{2.33}$$

Substituting Eqs. (2.31)–(2.33) to Eq. (2.29) yields

$$\begin{aligned} E_{interface} &= \int_0^{\lambda}\int_0^{2\pi} -\sigma\kappa f \mathrm{d}S = \int_0^{\lambda}\int_0^{2\pi} -\sigma\frac{\nabla^2 H}{|\nabla H|} f|\nabla H|\ \mathrm{d}\theta\mathrm{d}x \\ &= \int_0^{\lambda}\int_0^{2\pi} -\sigma\left[1 - \frac{n^2}{r^2} f + \alpha^2 f\right] f\ \mathrm{d}\theta\mathrm{d}x \\ &= \int_0^{\lambda}\int_0^{2\pi} -\sigma f\ \mathrm{d}\theta\mathrm{d}x + \int_0^{\lambda}\int_0^{2\pi} \sigma\left(n^2 + \alpha^2\right) f^2\ \mathrm{d}\theta\mathrm{d}x \\ &= \int_0^{\lambda}\int_0^{2\pi} \sigma\left(n^2 + \alpha^2\right) f^2\ \mathrm{d}\theta, \end{aligned} \tag{2.34}$$

and thus establishes $B = (n^2 + \alpha^2)$. We note that within the framework of spatial stability analysis considered herein, the streamwise wavenumber, α, differs for each of eigensolutions.

2.6. *Adjoint eigenfunction and group velocity*

In this study, we restrict our analysis to exponentially stable settings in which all eigensolutions of the spatial stability problem Eq. (2.12) decay in x. While the sign of the eigenvalue reveals the stability of the eigensolution in temporal analysis, the nonlinear spatial eigenvalue problem permits no such immediate classification. Existing approaches to identify the stability properties of spatial modes involve for instance iterative schemes such as the one applied by Lin & Chen (1998). In the present work, we directly determine the spatial stability of individual eigenfunctions by evaluating their group velocity,

$$c_g \equiv \frac{\partial \omega}{\partial \alpha}, \tag{2.35}$$

using information provided by the adjoint stability equations. More specifically, a positive spatial growth rate, i.e. a negative imaginary part of α, implies spatial growth if the group speed of the corresponding mode is positive. If the group speed of the eigenfunction is negative, it travels upstream and thus undergoes decay. Analogously, a mode with a negative spatial growth rate, i.e. a positive imaginary part of α will decay if its group speed is positive, and amplify if its group speed is negative. While iterative approaches require multiple solutions of the stability problem for each individual mode, the gradient information provided by the adjoint problem identifies the group speed of all eigensolutions after solving the linear system, Eq. (2.12) only once.

To proceed, we define the inner product $\langle a, b\rangle$ as the volume integrated dot product within the computational domain, $\int_\Omega a^{\mathsf{H}} b \, \mathrm{d}V$. The adjoint eigenfunctions, $\widehat{\boldsymbol{q}^\dagger}$, are the solution of the adjoint eigenvalue problem,

$$\alpha^* \mathsf{M}^{\mathsf{H}} \widehat{\boldsymbol{q}^\dagger} = \mathsf{L}^{\mathsf{H}} \widehat{\boldsymbol{q}^\dagger}, \tag{2.36}$$

where superscript * denotes complex conjugate. Solutions to the forward and adjoint eigenvalue problem satisfy a bi-orthogonality condition, so that upon proper normalization

$$\langle \widehat{\boldsymbol{q}^\dagger}_i, \ \mathsf{M}\widehat{\boldsymbol{q}}_j \rangle = \delta_{ij}. \tag{2.37}$$

To derive a relation for the group velocity, we apply a partial derivative with respect to ω to Eq. (2.12), yielding

$$\frac{\partial \alpha}{\partial \omega} \mathsf{M}\widehat{\boldsymbol{q}} + \alpha \mathsf{M} \frac{\partial \widehat{\boldsymbol{q}}}{\partial \omega} = \frac{\partial \mathsf{L}}{\partial \omega}\widehat{\boldsymbol{q}} + \mathsf{L}\frac{\partial \widehat{\boldsymbol{q}}}{\partial \omega}, \tag{2.38}$$

and implying that

$$\frac{\partial \alpha}{\partial \omega} \mathsf{M}\widehat{\boldsymbol{q}} = \frac{\partial \mathsf{L}}{\partial \omega}\widehat{\boldsymbol{q}}. \tag{2.39}$$

Multiplication by $\widehat{\boldsymbol{q}^\dagger}^{\mathsf{H}}$ gives

$$\widehat{\boldsymbol{q}^\dagger}^{\mathsf{H}} \frac{\partial \alpha}{\partial \omega} \mathsf{M}\widehat{\boldsymbol{q}} = \widehat{\boldsymbol{q}^\dagger}^{\mathsf{H}} \frac{\partial \mathsf{L}}{\partial \omega}\widehat{\boldsymbol{q}}, \tag{2.40}$$

which after integration over the computational domain becomes

$$\frac{\partial \alpha}{\partial \omega} \langle \widehat{\boldsymbol{q}^\dagger}, \mathsf{M}\widehat{\boldsymbol{q}} \rangle = \langle \widehat{\boldsymbol{q}^\dagger}, \frac{\partial \mathsf{L}}{\partial \omega}\widehat{\boldsymbol{q}} \rangle. \tag{2.41}$$

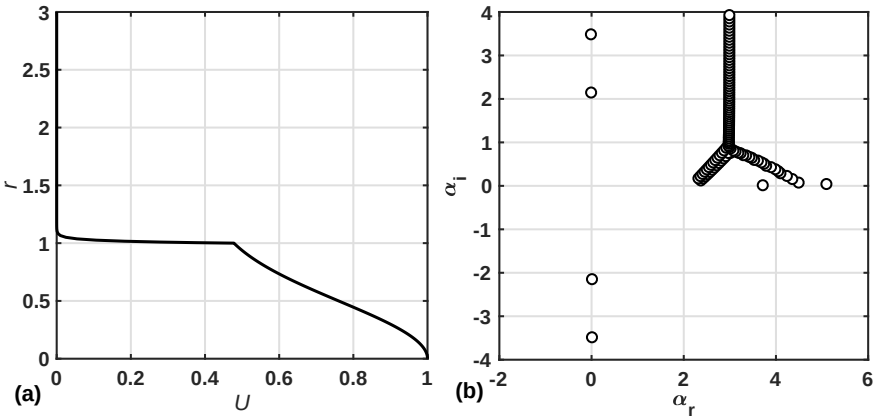

FIGURE 1. (a) Base flow of liquid jet in stationary gas. Velocity gradient changes at $r = 1$ due to the material interface is located at $r = 1$. (b) Eigenvalue spectrum in spatial linear stability analysis for $Re = 9825$, $We = 2881$, $m = 0.0115$, $\eta = 0.0015$, $n = 5$ and $\omega = 2.2$.

Applying the bi-orthogonality condition, Eq. (2.37), non-trivial cases with $i = j$, i.e. $\widehat{\boldsymbol{q}}^\dagger$ being the adjoint eigenfunction to $\widehat{\boldsymbol{q}}$, simplify Eq. (2.41) to

$$\frac{\partial \alpha}{\partial \omega} = \langle \widehat{\boldsymbol{q}}^\dagger, \frac{\partial \mathsf{L}}{\partial \omega} \widehat{\boldsymbol{q}} \rangle. \tag{2.42}$$

The group velocity of an eigenfunction $\widehat{\boldsymbol{q}}$, and by extension its exponential stability within the spatial stability framework, may thus be evaluated by the inner product with its corresponding adjoint eigenvector $\widehat{\boldsymbol{q}}^\dagger$,

$$\frac{\partial \omega}{\partial \alpha} = \left(\frac{\partial \alpha}{\partial \omega} \right)^{-1} = \langle \widehat{\boldsymbol{q}}^\dagger, \ \frac{\partial \mathsf{L}}{\partial \omega} \widehat{\boldsymbol{q}} \rangle. \tag{2.43}$$

3. Results

3.1. *Base flow and eigenvalue spectrum*

The flow configuration considered in this study is a synthetic analytical solution for a laminar, axisymmetric liquid jet as introduced in Boronin *et al.* (2013). Figure 1(a) presents the radial velocity profile. The material interface is located at $r = 1$. The velocity is continuous across the interface and satisfies a stress-continuity condition. The domain of the liquid phase, $0 \leq r \leq 1$, and that of gas phase, $1 \leq r \leq 3$, are discretized using Chebyshev collocation method. The number of collocation points used in each domain are $N_1 = 120$ in the liquid phase and $N_2 = 70$ in the gas phase. Convergence studies demonstrated that the computed results are insensitive to both the changes in the radial extent of the domain in the gas phase and the grid resolution in either domain. The eigenvalue spectrum computed in a spatial linear stability analysis is presented in Figure 1(b). In contrast to temporal stability analyses, the eigenvalues cover all four quadrants of the complex plane. We note that modes on the vertical α axis with $\alpha_r = 0$ may be considered spurious and ascribed to the inflation introduced in the solution of the polynomial eigenvalue problem, Eqs. (2.16)–(2.17).

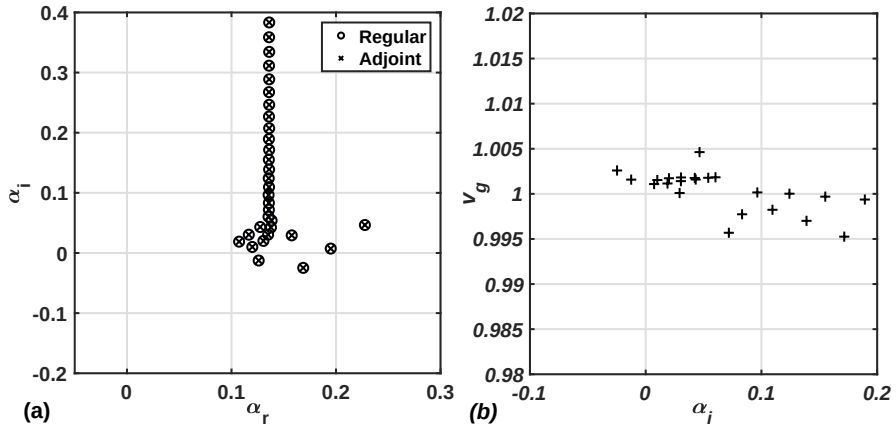

FIGURE 2. (a) Eigenvalue spectrum with two unstable and downstream propagating modes. (b) Group velocity evaluated with adjoint eigenfunctions. Positive group velocity for the modes with negative imaginary part of α_i denotes the stability of each mode.

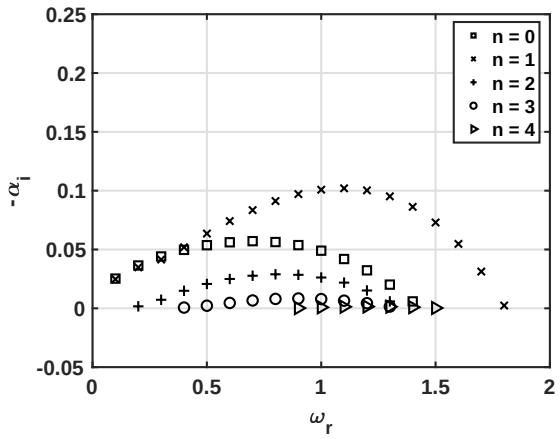

FIGURE 3. Unstable modes for different discrete azimuthal wavenumber. We excluded the discrete azimuthal number cases where exponentially unstable mode exists. Using adjoint eigenfunction to evaluate the stability of the eigenmodes, we can avoid iteration methods.

3.2. *Evaluation of the stability of eigenmodes*

As discussed in Section 2.6, the spatial stability problem impedes classification of the exponential stability of eigensolutions based on the sign of the eigenvalue. In this work, we thus evaluate the group velocity of the eigensolutions in determining their stability properties. Figure 2(a) shows the eigenvalue spectrum of $Re = 9825$, $We = 2881$, $m = 0.0115$, $\eta = 0.0015$, $n = 5$ and $\omega = 2.2$ after eliminating the spurious modes mentioned above. Two modes are shown to have a negative imaginary part of α. The group speed of the eigensolutions is presented in Figure 2(b), and shows that c_g is positive for all eigenfunctions. The two eigensolutions with negative α_i are thus indeed exponentially stable while all other modes with $\alpha_i > 0$ are stable. The present study focuses on exponentially stable settings for which all eigenfunctions decay in space. For the setting $Re = 8000$, $We = 1000$, $m = 0.01$, $\eta = 0.001$, Figure 3 presents the growth rates of the

most unstable mode as a function of the frequency, ω. For the given conditions, unstable modes are observed for $n = 0, 1, 2, 3$ and 4. The cases $n = 5$, 6 and 7 are exponentially stable, and will be focused upon in the following.

3.3. *Optimization problem*

Earlier investigations into non-exponential growth in two-fluid settings focused on the lift-up mechanism, which generates streamwise elongated perturbations of low frequency. For single-phase shear layers, the Orr mechanism is known as an alternative pathway for non-exponential amplification of disturbances (Orr 1907). Depending on the setting, the Orr mechanism may act independently or in conjunction with the lift-up effect (see e.g. Hack & Moin 2017). As documented by Jiménez (2013), the Orr mechanism produces cross-stream perturbation velocity from initially backward-leaning structures via their tilting in the flow direction by the mean shear. Similar to the lift-up effect, the gain in perturbation kinetic energy by the Orr mechanism is of a transient nature and eventually overcome by viscous decay. In contrast to the lift-up mechanism, the Orr mechanism generates scales on the order of the thickness of the shear layer which are much shorter in their streamwise extent.

The resulting amplification of interface energy is presented in Figure 4(a). As defined in Eq. (2.28), the objective functional G measures the ratio of the interface energy at the target position x for perturbations whose spatial evolution begins at $x_0 = 0$ and relates it to the total kinetic and interface energy of the perturbations at the initial position. The growth of the objective functional with x appears non-monotonic, and thus describes a deviation from the behavior known from single-phase boundary layer. This difference in behavior may be ascribed to characteristic differences between the present problem, and a wall-bounded shear flow. While the latter setting imposes no-slip condition at the wall on the perturbations, the material interface only imposes continuity of the stresses on the perturbations. Secondly, the material interface is coupled with radial perturbation velocity by a kinetic condition which allows perturbations normal to the interface. As a result, we observed a non-monotonic behavior in Figure 4(a) shows the maximum interface energy gain that we expect each corresponding streamwise location. Note that the horizontal axis of Figure 4(a,b) are target location, x_1, and streamwise location, x, respectively.

For the case $x = 11.8$, the interface potential energy is increased by a factor of 5.4 relative to initial total perturbation energy. Figure 4(b) presents the evolution of the absolute value of interface distortion, normalized by its initial value as a function of x. The maximum ratio for the absolute value of interface distortion at $x = 11.8$ is $|f(t)|/|f_0| \simeq 1042$. The evolution of the interface distortion shows a clearly non-monotonic trend, but continues to amplify up to $x = 11.8$. The non-monotonicity relates to a temporary redistribution between the interface and the velocity perturbations.

Both viscosity and surface tension have an appreciable effect on the amplification of the interface distortions. The influence of the Reynolds and Weber numbers on G is presented in Figure 5 for fixed $m = 0.01$ and $\eta = 0.001$. As an example, the ejection of a water jet into air through a nozzle of diameter $d = 100 \times 10^{-6}$ m with a velocity $v_{exit} = 100$ m/s corresponds to a Reynolds number of approximately 9000 and a Weber number of approximately 13000. The results indicate non-monotonic behavior with local maximum which become more prominent as the Reynolds number is increased.

The streamwise evolution of the optimal interface disturbances computed for the parameters $Re = 7500$, $We = 3000$, $m = 0.01$, $\eta = 0.001$, $n = 5$ and $\omega = 2.2$ is presented in Figure 6. Vectors represent the perturbation velocity in the streamwise and radial di-

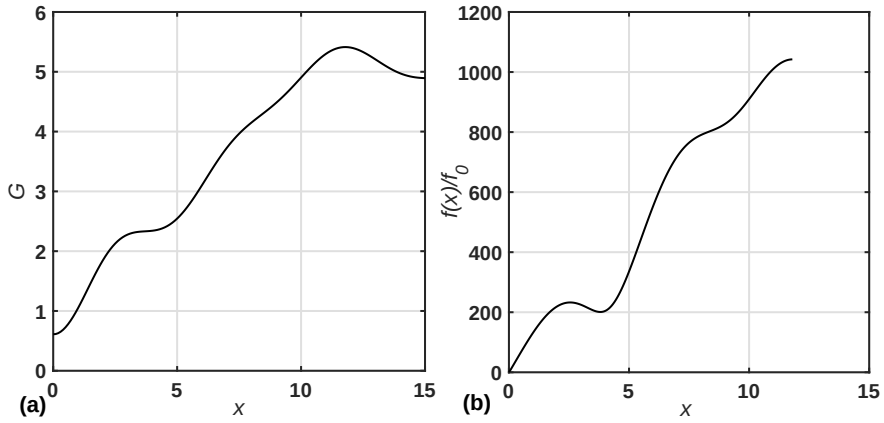

FIGURE 4. (a) Maximum energy gain expectation for each stream-wise location. Unlike the single phase transient growth analysis, existence of the free-surface give curved line for energy gain plot. (b) Ratio of the absolute value of interface disturbance eigenfunction from initial location to the point where G would get maximum value predicted by (a). Both (a) and (b) are computed with $Re = 7500$, $We = 3000$, $m = 0.01$, $\eta = 0.001$, $n = 5$ and $\omega = 2.2$.

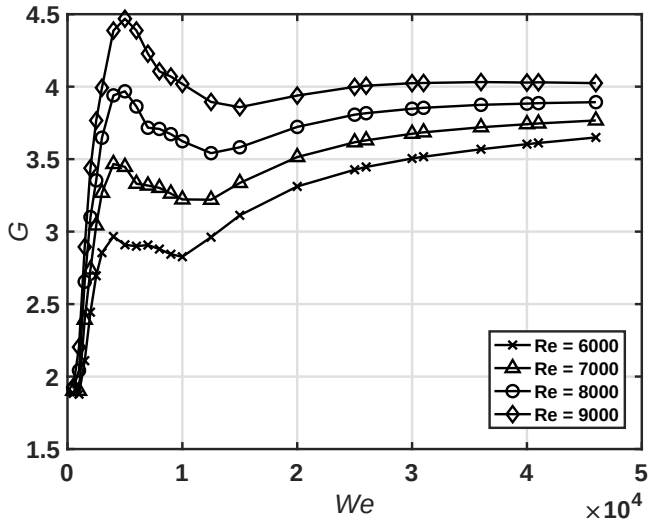

FIGURE 5. Energy gain versus We. We observe local maximum as We is increased and this maximum become dominant as Re is increased. With $m = 0.01$, $\eta = 0.001$ and $n = 6$, ω is chosen to give the maximum G for each pair of Re and We.

mensions, u_r, and contours show the azimuthal component of the perturbation velocity. The interface of the liquid jet is marked by solid circles. The results demonstrate the growth in the intensity of the perturbation velocities as the initially tilted fluid structure is reoriented by the mean shear. As a consequence, the distortion of the material surface is amplified and peaks at $x = 11.8$.

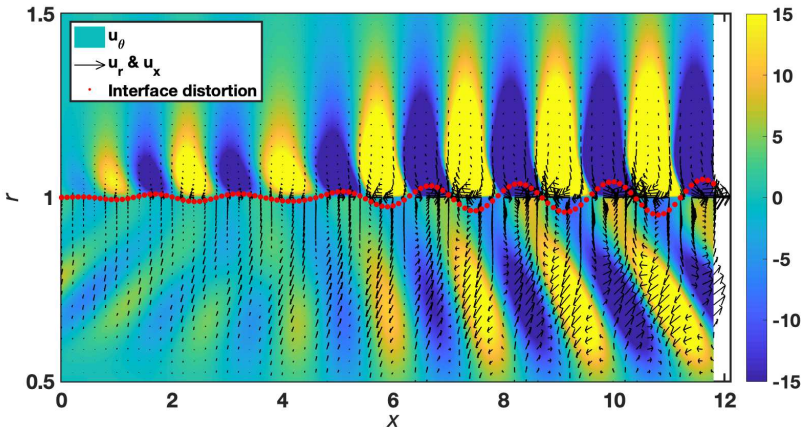

FIGURE 6. Physical representation of perturbations velocity and interface distortion of a liquid jet. All the eigenvectors are converted into physical space via inverse Fourier transform and plotted form the initial location to the point where defined energy norm is maximized. This was computed with $Re = 7500$, $We = 3000$, $m = 0.01$, $\eta = 0.001$, $n = 5$ and $\omega = 2.2$.

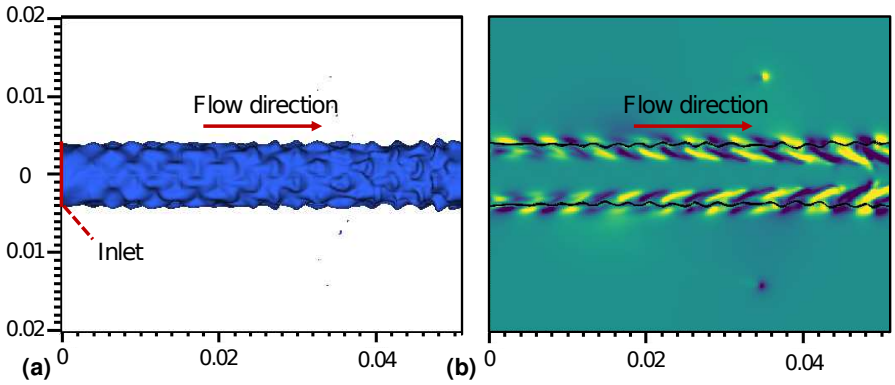

FIGURE 7. Realization of the linear stability analysis to get the most effective interface distortion. Basilisk (Popinet 2015, 2018) is employed for the simulation with initial perturbed condition predicted by linear stability analysis as an inlet condition. (a) VOF surface of value 0.5. (b) Azimuthal velocity perturbation, u_θ, and interface location as a black solid line. Note that tilting structure is observed in the liquid jet. Computed with $Re = 9825$, $We = 2881$, $m = 0.0115$, $\eta = 0.0015$, $n = 5$ and $\omega = 2.2$.

3.4. *Nonlinear simulation of optimal initial condition*

The initial condition computed with $Re = 9825$, $We = 2881$, $m = 0.0115$, $\eta = 0.0015$, $n = 5$ and $\omega = 2.2$ is used as an inlet condition of a simulation of the full two-fluid Navier-Stokes equations. An orthogonal structured grid of size $[N_x, N_y, N_z] = [1024 \times 512 \times 1024]$ and spatial extent $[L_x, L_y, L_z] = [0.32, 0.16, 0.16]$ is used. The diameter of the jet is $D = 0.0039$ and the inlet velocity at the centerline is $U_c = 1$ using the same base-flow profile as in the linear analyses. The spatial evolution of the flow is presented in Figures. 7(a,b) and confirms the mechanism identified with linear stability theory and the optimization of interface energy norm.

4. Conclusions

An alternative pathway for the generation of distortions of the material interface of a liquid jet has been demonstrated. The most effective disturbances exploit the Orr mechanism to amplify the magnitude of the initial interface distortion appreciably. The analysis employs linear stability theory in a spatial framework and identifies optimal disturbances based on an objective functional in terms of the surface-tension energy of the material interface. The results predicted by linear theory are verified in simulations of the full multi-phase Navier-Stokes equations using the open-source code Basilisk. The present study thus demonstrates the possibility of triggering the onset of the atomization process of a liquid jet in the absence of exponential instability.

Acknowledgments

Hanul Hwang is funded by the Franklin P. and Caroline M. Johnson Fellowship. The authors gratefully thank to Prof. Parviz Moin for his insightful comments on the investigation. The authors also thank Michael Karp and Ronald Chan for fruitful discussions.

REFERENCES

Boronin, S. A., Healey, J. J. & Sazhin, S. S. 2013 Non-modal stability of round viscous jets. *J. Fluid Mech.* **716**, 96–119.

Foures, D. P. G., Caulfield, C. P & Schmid, P. J. 2012 Variational framework for flow optimization using seminorm constraints. *Phys. Rev.* **86**, 026306.

Gustavsson, L. H. 1991 Energy growth of three-dimensional disturbances in plane Poiseuille flow. *J. Fluid Mech.* **224**, 241–260.

Hack, M. J. P. & Moin, P. 2017 Algebraic disturbance growth by interaction of Orr and lift-up mechanisms. *J. Fluid Mech.* **829**, 112–126.

Hoyt, J. W. & Taylor, J. J. 1977 Waves on water jets. *J. Fluid Mech.* **83**, 119–127.

Hu, H. H. & Joseph, D. D. 1989 Lubricated pipelining: stability of core–annular flow. Part 2. *J. Fluid Mech.* **205**, 359–396.

Huh, K. Y., Lee, E. and Koo, J.-Y.1998 Diesel spray atomization model considering nozzle exit turbulence conditions. *At. Sprays* **8**, 453–469.

Hwang, H. & Hack, M. J. P. 2018 The most effective interface disturbance of a round liquid jet. *Annual Research Briefs*, Center for Turbulence Research, Stanford University, pp. 79–91.

Jiménez, J. 2013 How linear is wall-bounded turbulence? *Phys. Fluids* **25**, 110814.

Jiménez-González, J. I. & Brancher, P. 2017 Transient energy growth of optimal streaks in parallel round jets. *Phys. Fluids* **29**, 114101.

Kim, D. & Moin, P. 2011 Numerical simulation of the breakup of a round liquid jet by a coaxial flow of gas with a subgrid Lagrangian breakup model. *Annual Research Briefs*, Center for Turbulence Research, Stanford University, pp. 15–30.

Lasheras, J. C. & Hopfinger, E. J. 2000 Liquid jet instability and atomization in a coaxial gas stream. *Annu. Rev. Fluid Mech.* **32**, 275–308.

Lin, S. P. & Chen, J. N. 1998 Role played by the interfacial shear in the instability mechanism of a viscous liquid jet surrounded by a viscous gas in a pipe. *J. Fluid Mech.* **376**, 37–51.

Lin, S. P. & Ibrahim, E. A. 1990 Instability of a viscous liquid jet surrounded by a viscous gas in a vertical pipe. *J. Fluid Mech.* **218**, 641–658.

Malik, S. V. & Hooper, A. P. 2007 Three-dimensional disturbances in channel flows. *Phys. Fluids* **19**, 052102.

Marmottant, P. & Villermaux, E. 2004 On spray formation. *J. Fluid Mech.* **498**, 73–111.

Orr, W. M'F. 1907 The stability or instability of the steady motions of a perfect liquid and of a viscous liquid. part II: a viscous liquid. *Proc. R. Ir. Acad.* **27**, 69–138.

Popinet, S. 2015 A quadtree-adaptive multigrid solver for the Serre–Green–Naghdi equations. *J. Comput. Phys.* **302**, 336–358.

Popinet, S. 2018 Numerical models of surface tension. *Annu. Rev. Fluid Mech.* **50**, 49–75.

Preziosi, L., Chen, K. & Joseph, D. D. 1989 Lubricated pipelining: stability of core-annular flow. *J. Fluid Mech.* **201**, 323–356.

Schmid, P. J. & Henningson, D. S. 1994 Optimal energy density growth in Hagen-Poiseuille flow. *J. Fluid Mech.* **277**, 197–225.

Schmidt, D. P., Nouar, I., Senecal, P. K. Rutland, C. J., Martin, J. K. & Reitz, R. D. 1999 Pressure-swirl atomization in the near field. *SAE Technical Paper Series* 1999-01-0496.

Senecal, P. K. Schmidt, D. P., Nouar, I., Rutland, C. J., Reitz, R. D. & Corradini, M. L. 1999 Modeling high-speed viscous liquid sheet atomization. *Int. J. Multiph. Flow* **25**, 1073–1097.

South, M. J. & Hooper, A. P. 1999 Linear growth in two–fluid plane Poiseuille flow. *J. Fluid Mech.* **381**, 121–139.

Trefethen, L. N., Trefethen, A. E., Reddy, S. C. & Driscoll, T. A. 1993 Hydrodynamic stability without eigenvalues. *Science* **261**, 578–584.

van Noorden, T. L., Boomkamp, P. A. M., Knaap, M. C. & Verheggen, T. M. M. 1998 Transient growth in parallel two-phase flow: analogies and differences with single-phase flow. *Phys. Fluids* **10**, 2099–2101.

Yecko, P. A. & Zaleski, S. 2005 Transient growth in two-phase mixing layers. *J. Fluid Mech.* **528**, 43–52.